

NIKA 150 GHz polarization observations of the Crab nebula and its Spectral Energy Distribution

A. Ritacco^{1,8*}, J.F. Macías-Pérez¹, N. Ponthieu¹⁰, R. Adam^{1,2,18}, P. Ade⁵, P. André⁴, J. Aumont¹⁴, A. Beelen⁶, A. Benoît⁷, A. Bideaud⁷, N. Billot⁸, O. Bourrion¹, A. Bracco^{4,21}, M. Calvo⁷, A. Catalano¹, G. Coiffard³, B. Comis¹, A. D'Addabbo^{7,9}, M. De Petris⁹, F.-X. Désert¹⁰, S. Doyle⁵, J. Goupy⁷, C. Kramer⁸, G. Lagache¹¹, S. Leclercq³, J.-F. Lestrade¹⁷, P. Mauskopf^{5,12}, F. Mayet¹, A. Maury⁴, A. Monfardini⁷, F. Pajot⁶, E. Pascale⁵, L. Perotto¹, G. Pisano⁵, M. Rebolo-Iglesias¹, V. Revéret⁴, L. Rodriguez⁴, C. Romero³, H. Roussel¹⁶, F. Ruppin¹, K. Schuster³, A. Sievers⁸, G. Siringo¹⁹, C. Thum⁸, S. Triqueneaux⁷, C. Tucker⁵, H. Wiesemeyer²⁰, and R. Zylka³

¹ Laboratoire de Physique Subatomique et de Cosmologie, Université Grenoble Alpes, CNRS/IN2P3, 53, avenue des Martyrs, Grenoble, France

² Laboratoire Lagrange, Université Côte d'Azur, Observatoire de la Côte d'Azur, CNRS, Blvd de l'Observatoire, CS 34229, 06304 Nice cedex 4, France

³ Institut de RadioAstronomie Millimétrique (IRAM), Grenoble, France

⁴ Laboratoire AIM, CEA/IRFU, CNRS/INSU, Université Paris Diderot, CEA-Saclay, 91191 Gif-Sur-Yvette, France

⁵ Astronomy Instrumentation Group, University of Cardiff, UK

⁶ Institut d'Astrophysique Spatiale (IAS), CNRS and Université Paris Sud, Orsay, France

⁷ Institut Néel, CNRS and Université Grenoble Alpes, France

⁸ Institut de RadioAstronomie Millimétrique (IRAM), Granada, Spain

⁹ Dipartimento di Fisica, Sapienza Università di Roma, Piazzale Aldo Moro 5, I-00185 Roma, Italy

¹⁰ Univ. Grenoble Alpes, CNRS, IPAG, 38000 Grenoble, France

¹¹ Aix Marseille Université, CNRS, LAM (Laboratoire d'Astrophysique de Marseille) UMR 7326, 13388, Marseille, France

¹² School of Earth and Space Exploration and Department of Physics, Arizona State University, Tempe, AZ 85287

¹³ Université de Toulouse, UPS-OMP, Institut de Recherche en Astrophysique et Planétologie (IRAP), Toulouse, France

¹⁴ CNRS, IRAP, 9 Av. colonel Roche, BP 44346, F-31028 Toulouse cedex 4, France

¹⁵ University College London, Department of Physics and Astronomy, Gower Street, London WC1E 6BT, UK

¹⁶ Institut d'Astrophysique de Paris, Sorbonne Universités, UPMC Univ. Paris 06, CNRS UMR 7095, 75014 Paris, France

¹⁷ LERMA, CNRS, Observatoire de Paris, 61 avenue de l'Observatoire, Paris, France

¹⁸ Centro de Estudios de Física del Cosmos de Aragón (CEFCA), Plaza San Juan, 1, planta 2, E-44001, Teruel, Spain

¹⁹ Joint ALMA Observatory & European Southern Observatory, Alonso de Córdova 3107, Vitacura, Santiago, Chile

²⁰ Max Planck Institute for Radio Astronomy, 53111 Bonn, Germany

²¹ Nordita, KTH Royal Institute of Technology and Stockholm University, Roslagstullsbacken 23, 10691 Stockholm, Sweden

Received March 7, 2018 / Accepted –

ABSTRACT

The Crab nebula is a supernova remnant exhibiting a highly polarized synchrotron radiation at radio and millimeter wavelengths. It is the brightest source in the microwave sky with an extension of 7 by 5 arcminutes and commonly used as a standard candle for any experiment which aims at measuring the polarization of the sky. Though its spectral energy distribution has been well characterized in total intensity, polarization data is still lacking at millimetre wavelengths. We report in this paper high resolution (18'' FWHM) observations of the Crab nebula in total intensity and linear polarization at 150 GHz with the NIKA camera. NIKA, operated at the IRAM 30 m telescope from 2012 to 2015, is a camera made of Lumped Element Kinetic Inductance Detectors (LEKIDs) observing the sky at 150 and 260 GHz. From these observations we are able to reconstruct the spatial distribution of the Crab nebula polarization degree and angle, which is found to be compatible with previous observations at lower and higher frequencies. Averaging across the source and using other existing data sets we find that the Crab nebula polarization angle is consistent with being constant over a wide range of frequencies with a value of $-87.5^\circ \pm 0.3$ in Galactic coordinates. We also present the first estimation of the Crab nebula Spectral Energy Distribution polarized flux in a wide frequency range: 30-353 GHz. Assuming a single power law emission model we find that the polarization spectral index $\beta_{pol} = -0.35 \pm 0.03$ is compatible with the intensity spectral index $\beta = -0.324 \pm 0.001$.

Key words. Techniques: Crab nebula – Tau A – polarization – KIDs – individual: NIKA

1. Introduction

The Crab nebula (or Tau A) is a plerion-type supernova remnant emitting a highly polarized signal (Weiler & Panagia 1978;

Michel et al. 1991). Referring to Hester (2008), from inside out the Crab consists of a pulsar, the synchrotron nebula, a bright expanding shell of thermal gas, and a larger very faint freely expanding supernova remnant.

Near the center of the nebula a shock is observed as formed by the jet thermalized and pulsar's ultra-relativistic wind which

* Corresponding author: Alessia Ritacco, ritacca@iram.es

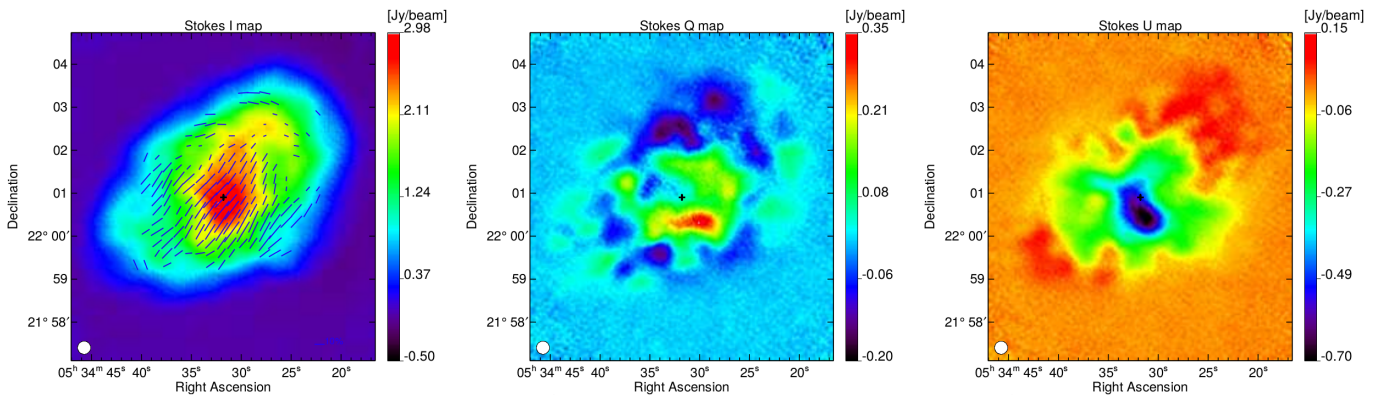


Fig. 1. From left to right: Crab nebula Stokes I , Q and, U maps shown here in Equatorial coordinates obtained at 150 GHz with the NIKA camera. Polarization vectors, indicating both the polarization degree and the orientation, are over-plotted in blue on the intensity map where the polarization intensity satisfies $I_{\text{pol}} > 3\sigma_{I_{\text{pol}}}$ and $I_{\text{pol}} > 0.1 \text{ Jy/beam}$. In each map, the NIKA FWHM is shown as a white disk in the bottom left-hand corner and the cross marks the pulsar position.

is confined by the thermal ejecta from the explosion (Weisskopf et al. 2000; Wiesemeyer et al. 2011). The synchrotron emission from the nebula is observed in the radio frequency domain as powered by the pulsar located at equatorial coordinates (J2000) $R.A. = 5^{\circ}34'31.9383014s$ and $Dec. = 22^{\circ}0'52.17577''$ (Lobanov et al. 2011) through its jet.

The polarization of the Crab nebula radio emission, discovered in 1957 independently by Mayer et al. (1957) and Kuz'min & Udal'Tsov (1959), has confirmed the synchrotron emission is the underlying mechanism.

Today the Crab nebula is perhaps the most observed object in the sky beyond our own solar system (Hester 2008) and often used as calibrator by new instruments. It is also quite isolated with low background diffuse emission.

In particular it is the most intense polarized astrophysical object in the microwave sky at angular scales of few arcminutes and for this reason it is chosen not only for high resolution cameras but also for the calibration of CMB (Cosmic Microwave Background) polarization experiments, which have beamwidths comparable to the extension of the source. Indeed, upcoming CMB experiments aiming at measuring the primordial B -modes require an accurate determination of the foreground emissions to the CMB signal and a high control of systematic effects. The Crab nebula has already been used for polarization cross-check analysis in the frequency range from 30 to 353 GHz (Weiland et al. 2011; Planck Collaboration et al. 2016a).

High angular resolution observations from the XPOL experiment (Thum et al. 2008) at the IRAM 30 m telescope have revealed the spatial distribution of the Crab Nebula in total intensity and polarization at 90 GHz with an absolute accuracy of 0.5° in the polarization angle (Aumont et al. 2010). This observation has also shown that the polarization spatial distribution varies from the source peak to the edges of the source and evidences the need of an accurate study at high resolution in a large frequency range to be able to use this source as a calibrator for future polarization experiments.

Previous studies (Macías-Pérez et al. 2010) of the total Spectral Energy Distribution (SED) have shown a spectrum well described by a single synchrotron component at radio and mm wavelengths and predict negligible variations in polarization fraction and angle in the frequency range of interest for CMB studies.

Observations of the Crab nebula polarization have been performed with the NIKA camera (Monfardini et al. 2010; Cata-

lano et al. 2014; Monfardini et al. 2014) at the IRAM 30 m telescope during the observational campaign of February, 2015. A first overview of the NIKA/30m (NIKA from here on) Crab polarization observations, focusing on instrumental characterization of the polarization system, was given in Ritacco et al. (2016). In this paper we go a step further in the analysis by combining NIKA observations with published values at other frequencies, and spanning different angular resolutions, to trace the SED in total intensity and polarization of the Crab nebula. As far for polarization we use observations from the WMAP satellite at 23, 33, 41, 61 and 94 GHz (Weiland et al. 2011), from the Planck satellite at 30, 44, 70, 100, 143, 217, 353 GHz and from XPOL/30m (XPOL from here on) at 90 GHz (Aumont et al. 2010) and POLKA/APEX (POLKA from here on) at 345 GHz (Wiesemeyer et al. 2014).

The paper is organized as follows: in Sec. 2 the intensity and polarization maps obtained with the NIKA camera are presented together with the polarization degree and angle spatial distributions; Sec. 3 presents the reconstruction of the polarization properties of the Crab nebula in well defined regions; Sec. 4 presents the Crab nebula SED in total intensity and polarization; in Sec. 5 we present our conclusions.

2. NIKA observations of the Crab Nebula

2.1. NIKA camera and polarization setup

NIKA is a dual band camera observing the sky in total intensity and polarization at 150 and 260 GHz with 18 arcsec and 12 arcsec FWHM resolution, respectively. It has a Field-of-View (FoV) of $1.8'$ at both wavelengths. It was operated at the IRAM 30 m telescope between 2012 and 2015. A detailed description of the NIKA camera can be found in Monfardini et al. (2010, 2011) and Catalano et al. (2014).

In addition to total power observations, NIKA was also a test bench for the polarization system of the final instrument NIKA2 (Calvo et al. 2016; Catalano et al. 2016; Adam et al. 2018), which was installed at the telescope in October, 2015. The polarization setup of NIKA consists in a continuously rotating metal mesh half wave plate (HWP) followed by an analyzer, both at room temperature and placed in front of the entrance window of the cryostat. The NIKA Lumped Elements Kinetic Inductance Detectors (LEKIDs) are not intrinsically sensitive to polarization. The HWP rotates at 2.98 Hz allowing a modulation of the

polarization signal at 4×2.98 Hz while the typical telescope scanning speed is equal to 26.23 arcsec/s. These conditions provide a quasi-simultaneous measure of Stokes parameters I , Q and U per beam and place the polarized power in the frequency domain far from the low frequency electronic noise and the atmospheric fluctuations. [Ritacco, A. et al. \(2017\)](#) give more details on the NIKA polarization capabilities and describes the performance of the instrument at the telescope. In particular the sensitivity of the NIKA camera in polarization mode was estimated to be $50 \text{ mJy.s}^{1/2}$ at 150 GHz.

NIKA has provided the first polarization observations performed with Kinetic Inductance Detectors, confirming that KIDs are a suitable detector technology for the development also of the next generation of polarization sensitive experiments.

2.2. NIKA observations

Observations of the polarized emission from the Crab nebula with the NIKA camera were performed at the IRAM 30 m telescope in February, 2015. The average opacity at 150 GHz was $\tau = 0.2$. Fig. 1 shows the Stokes I , Q and U maps obtained by a co-addition of 14 maps of 8×6 arcminutes for a total observation time of ~ 2.4 hours. The rms calculated on jack-knife noise maps is 36 mJy/beam on Stokes I and 31 mJy/beam on polarization maps Stokes Q and U . The maps were performed in equatorial coordinates in four different scan directions: 0° , 90° , 120° , 150° . This allowed us to have the best mapping with different position angles.

To obtain the Stokes I , Q , and U Crab nebula maps in Equatorial coordinates, we have used a dedicated polarization data reduction pipeline ([Ritacco, A. et al. 2017](#)), which is an extension of the total intensity NIKA pipeline ([Catalano et al. 2014](#); [Adam et al. 2014](#)). The main steps of the polarization pipeline are summarized below.

1. Subtraction of the HWP induced parasitic signal, which is modulated at harmonics of the HWP rotation frequency and represents the most tedious noise contributing to the polarized signal.
2. Reconstruction of the Stokes I , Q and U time ordered information (TOI) from the raw modulated data. This is achieved using a demodulation procedure consisting in a lock-in around the fourth harmonic of the HWP rotation frequency, where the polarization signal is located.
3. Subtraction of the atmospheric emission in the demodulated TOIs using decorrelation algorithms. In polarization, the HWP modulation reduces significantly the atmospheric contamination and there is no need to further decorrelate the Q and U TOI's from residual atmosphere. By contrast, in intensity the atmospheric emission fully dominates the signal and, to recover the large angular scales, we use the 260 GHz band as an atmosphere dominated band like in [Adam et al. \(2014\)](#). This decorrelation impacts the reconstructed Stokes maps via a transfer function. We have estimated this function with simulated observations of diffuse emission that were passed through the data reduction pipeline, with the exact same scanning, sample flagging and data processing as real data. We found that the power spectrum of the output maps match that of the input one to better than 1% (5%) on scales smaller (resp. larger) than $\sim 1'$, see Fig. 2. Its moderate effect on large angular scales is further reduced with the subtraction of a zero level for the photometry (see below), so the impact of the data processing is thus negligible compared to uncertainties on absolute calibration on small scales. In the

following, we therefore neglect the impact of this transfer function.

4. Correction of the intensity-to-polarization-leakage-effect, which was identified in observations of unpolarized sources like the planet Uranus. For point sources the effect was about 3% peak-to-peak, while for extended sources like the Crab nebula it has been found to be the order of 0.5% peak-to-peak. [Ritacco, A. et al. \(2017\)](#) describe the algorithm of leakage correction developed specifically for NIKA polarization observations. Applying this algorithm to Uranus observations the instrumental polarization is reduced to 0.6% of the total intensity I .
5. Projection of the demodulated and decorrelated Stokes I , Q , and U TOIs into Stokes I , Q and U equatorial coordinates maps.

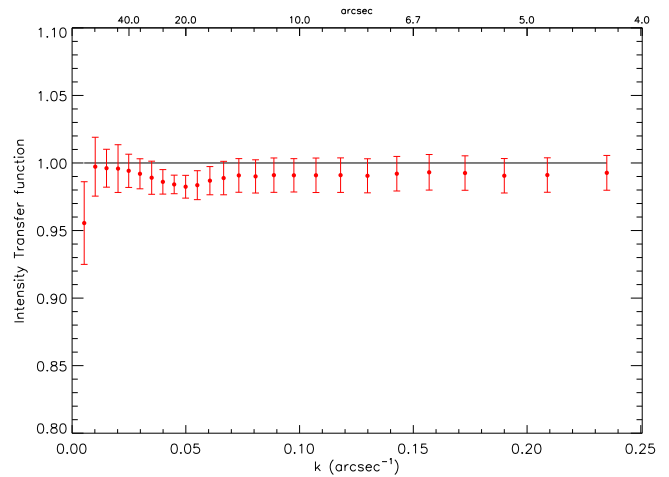


Fig. 2. Transfer function of the data processing in total intensity.

2.3. Crab polarization properties

In this section we discuss the polarization properties of the source in terms of polarization degree p and angle ψ , which are defined through the Stokes parameters I , Q , and U as follows:

$$p = \frac{\sqrt{Q^2 + U^2}}{I} \quad \text{and} \quad \psi = \frac{1}{2} \arctan \frac{U}{Q}. \quad (1)$$

The polarization angle follows the IAU convention, which counts East from North in the equatorial coordinate system.

These definitions are not linear in I , Q and U and therefore, the observational uncertainties have to be carefully considered, i.e. p and ψ are noise biased. [Simmons et al. \(1980\)](#); [Simmons & Stewart \(1985\)](#); [Montier et al. \(2015\)](#) proposed analytical solutions to correct for this bias. For intermediate and high S/N ratio the polarization degree and its uncertainty read:

$$p = \frac{\sqrt{Q^2 + U^2 - \sigma_Q^2 - \sigma_U^2}}{I}, \quad \sigma_p = \frac{\sqrt{Q^2 \sigma_Q^2 + U^2 \sigma_U^2 + p^4 I^2 \sigma_I^2}}{p I^2}. \quad (2)$$

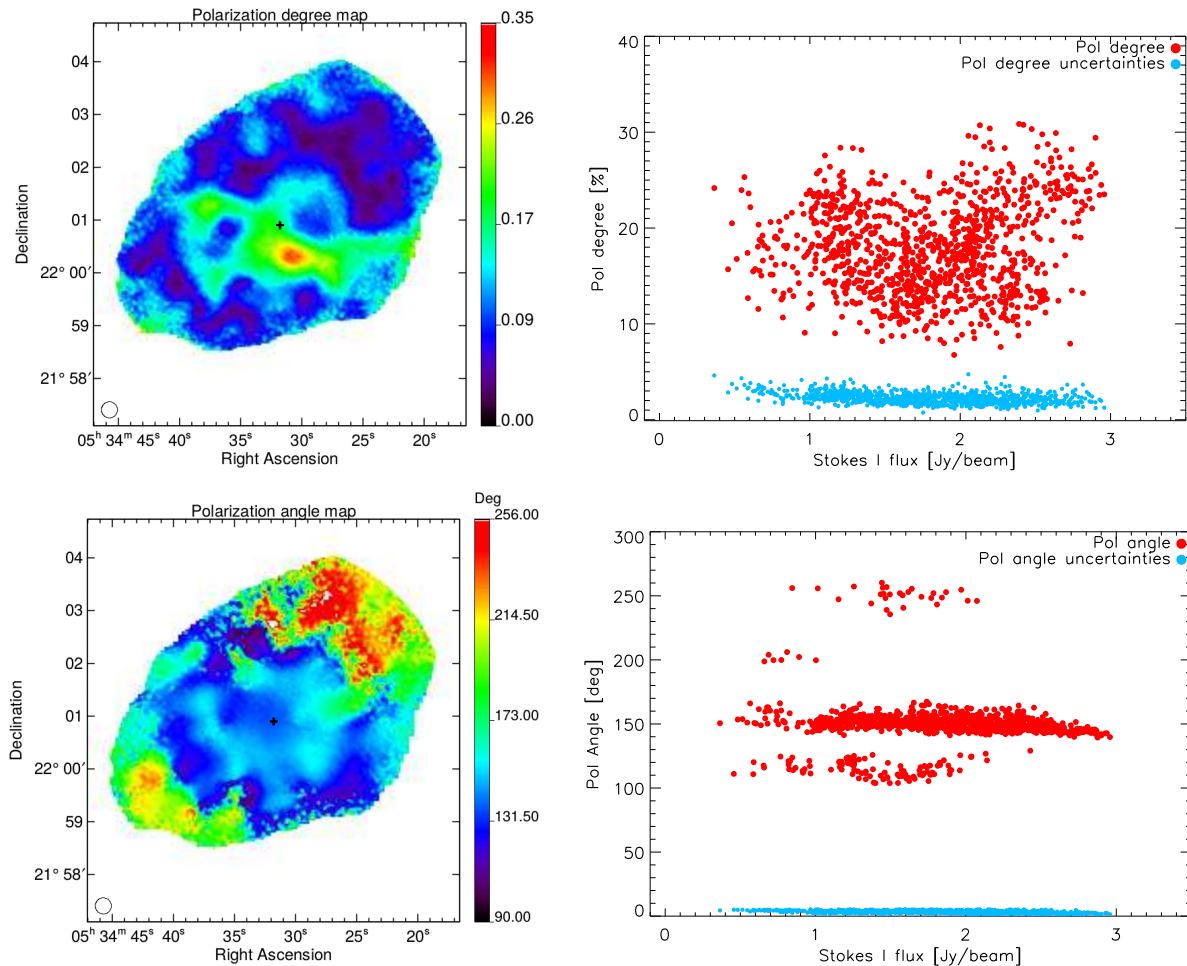


Fig. 3. *Top:* The left panel shows the polarization degree map p , uncorrected for noise bias, of the Crab nebula. The right panel shows the noise bias corrected p values as a function of total intensity map (Stokes I). The condition $I_{\text{pol}} > 5\sigma_{I_{\text{pol}}}$ is satisfied for those values. *Bottom:* on the left we present the polarization angle map ψ (Equatorial coordinates system) of the Crab nebula. On the right panel the distribution of ψ values is represented as a function of the total intensity in the case of very high S/N ratio where $I_{\text{pol}} > 5\sigma_{I_{\text{pol}}}$. The cyan dots represent the uncertainties calculated as the dispersion between different observational scans. The black cross marks the pulsar position on the maps.

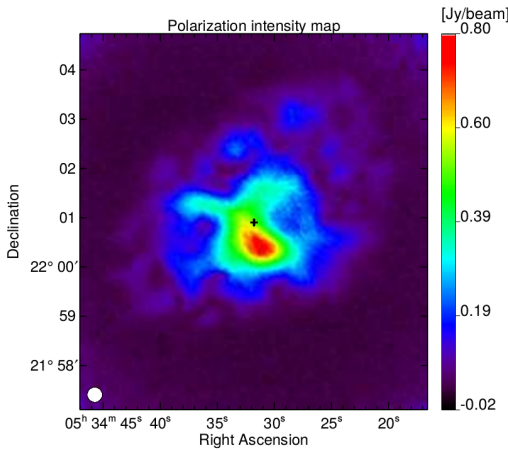


Fig. 4. NIKA polarized intensity map of the Crab nebula at 150 GHz. The map shows high polarized emission reaching a value of 0.8 Jy beam^{-1} . The telescope beam FWHM is shown in the lower left. The black cross marks the pulsar position.

Furthermore, the polarization angle in a high S/N regime can be approximated by Eq. 1 with the uncertainty

$$\sigma_\psi = \frac{\sqrt{Q^2\sigma_Q^2 + U^2\sigma_U^2}}{2(pI)^2}. \quad (3)$$

The spatial distribution map of the polarization degree p of the Crab nebula without noise bias correction is presented on the top left panel of Fig. 3. Notice that we have set to 0 the pixels for which the total intensity is lower than 0.1 Jy/beam to avoid the divergence of p . Same has been done for the polarization angle map (bottom left of Fig. 3.)

The polarization degree p reaches a value of $19.8 \pm 0.7 \%$ at the peak of the total intensity, which is consistent with what is observed on the top right panel of Fig. 3, where the variation of p as a function of the Stokes I is shown. Here the p values have been noise bias corrected and satisfy the condition $I_{\text{pol}} = \sqrt{Q^2 + U^2} > 5\sigma_{I_{\text{pol}}}$. The distribution of the polarization degree appears highly dispersed around a mean value of 20%. These points are mostly located around the peak of Stokes I . The spatial variation of p highlights the interest of high resolution polarization observations of the Crab nebula.

The bottom left panel of Fig. 3 shows the spatial distribution of polarization angle ψ . As discussed in Ritacco, A. et al. (2017)

a 1.8° uncertainty must be considered in the polarization angle coming from the determination of the HWP zero position, corresponding to its optical axis in the *NIKA* cabin reference frame. An uncertainty of 0.5° must be considered due to the leakage effect subtraction, which has been estimated from the comparison of the maps before and after leakage correction. We observe a relatively constant polarization angle $140^\circ < \psi_{\text{eq}} < 150^\circ$ represented here in equatorial coordinates, except for the northern-east region where the averaged angle is around 250° , and some inner regions with lower polarization angle. These values are confirmed by the bottom right panel that shows the polarization angle distribution as a function of total intensity satisfying the condition $I_{\text{pol}} > 5\sigma_{I_{\text{pol}}}$.

The sudden change of polarization angle on the northern region was already observed by the XPOL experiment at 90 GHz (Aumont et al. 2010). This together with the variation of the polarization fraction discussed above confirms the need of high angular resolution observations at low and high frequencies for a good understanding of the Crab polarized emission properties. High resolution observations give the possibility to estimate the polarization properties at different scales and compare with low resolution experiments, like CMB experiments.

We present in Fig. 4 the 150 GHz Crab polarization intensity map I_{pol} uncorrected for noise bias. We observe a peak at 0.8 Jy beam^{-1} and the polarization decreases towards the edges of the nebula.

2.4. Comparison to other high resolution experiments

Following previous studies, we compare here *NIKA* results at the pulsar position and at Stokes I map peak with high angular resolution experiments such as POLKA, XPOL and SCUPOL/JCMT (SCUPOL from here on). These experiments observed at wavelengths of $870 \mu\text{m}$, 3 mm and $850 \mu\text{m}$, respectively. Tab. 1 reports the measurement of the polarization properties, degree and angle, obtained by these experiments (Wiesemeyer et al. 2014). At the pulsar position we observe fair agreement in the polarization angle between POLKA, SCUPOL and *NIKA*. However, in terms of polarization degree there is not clear consistency. At the position of the peak in total intensity, *NIKA* shows a low polarization degree, but still consistent with SCUPOL and XPOL, the last has been recalculated on the maps published in Aumont et al. (2010). Some of the discrepancies observed in Tab. 1 may come from the different pixel resolution of the maps. Indeed being the pixel size different for each map, the computation of the values at the Stokes I peak or at the pulsar position is misleading.

3. Total intensity and polarization fluxes

We compute the total flux across the Crab nebula, which has an extent of about $5' \times 7'$ as shown in Fig. 1. We use standard aperture photometry techniques to calculate the flux as shown on the top panel of Fig. 5. We use as center position the center of the map with equatorial coordinates (J2000) $R.A. = 5^h34^m31.95s$ and $Dec. = 22^{\circ}0'52.1''$. A zero level in the map, calculated as the mean of the signal measured on an external annular ring region (see bottom panel of Fig. 5) of radius $4' < R < 4.5'$, has been subtracted from the map. The total signal estimated is $209.9 \pm 1.0 \pm 5.1 \pm 21.0 \text{ Jy}$. The first uncertainty term accounts for statistical uncertainties computed from fluctuations of the signal at large radii. The second uncertainty accounts for the difference between two sets of jack-knife noise maps. The latter one accounts for the absolute calibration error of 10%. We use

		$I \text{ [Jy]}$	$p \text{ [%]}$	$\psi_{\text{eq}} \text{ [}^\circ\text{]}$
Pulsar	POLKA	1.63	25.3 ± 3.0	145.1 ± 3.3
	XPOL		13.9 ± 0.6	158.1 ± 0.5
	SCUPOL		14.3 ± 1.8	140.0 ± 2.8
	<i>NIKA</i>	1.2 ± 0.13	18.2 ± 2.4	$137.8 \pm 0.5 \pm 2.3$
Peak	POLKA	1.72	25.0 ± 3.1	151.7 ± 3.5
	XPOL		21.0 ± 1.2	149.0 ± 1.4
	SCUPOL		18.7 ± 1.5	146.1 ± 2.1
	<i>NIKA</i>	1.22 ± 0.12	20.3 ± 2.5	$140.0 \pm 0.1 \pm 2.3$

Table 1. Values estimated by POLKA ($870 \mu\text{m}$), XPOL (3 mm), SCUPOL ($850 \mu\text{m}$) reported in Wiesemeyer et al. (2014) and *NIKA* (this paper) at the pulsar and peak position, respectively. The FWHM for these four experiments are $20''$, $27''$, $20''$ and $18.2''$, respectively. Notice that only the polarization degree value of XPOL at the peak position is found different w.r.t Wiesemeyer et al. (2014) and it has been recalculated directly on the maps published in Aumont et al. (2010). For *NIKA* the position of the pulsar, represented on the maps by a black cross, refers to Lobanov et al. (2011). The position of the peak of the total intensity measured on *NIKA* maps has equatorial coordinates (J2000) $R.A. = 5^h34^m32.3804s$ and $Dec. = 22^{\circ}0'44.0982''$. The polarization angle is given here in Equatorial coordinates. A systematic angle uncertainty of 2.3° is considered. A total calibration error of 10% has been accounted for and propagated to the polarization estimates.

Uranus for absolute point source flux calibration. The flux of the planet is estimated from a frequency dependent model of the planet brightness temperature as described in Moreno (2010). This model is integrated over the *NIKA* bandpasses for each channel, and it is assumed to be accurate at the 5% level. The final absolute calibration factor is obtained by fitting the amplitude of a Gaussian function of fixed angular size on the reconstructed maps of Uranus, which represents the main beam. For the polarization observational campaign of February 2015 this uncertainty is estimated to be 5% for the *NIKA* 2.05 mm channel (150 GHz) (Ritacco, A. et al. 2017). Nevertheless, as described in Adam et al. (2014); Catalano et al. (2014), by integrating the Uranus flux up to 100 arcsec, we observe that the total solid angle covered by the beam is larger than the Gaussian best-fit of the main beam by a factor of 28%. As a consequence we account for this factor in the estimation of the fluxes. Moreover, Adam et al. (2014) estimated the uncertainty on the solid angle of the main beam to be 4%. Finally, the overall calibration error is estimated to be about 10%, by considering also the uncertainties on the side lobes.

The polarization efficiency factor estimated across the *NIKA* 2.05 mm spectral band and reported in Ritacco, A. et al. (2017) is $\rho_{\text{pol}} = 0.9941 \pm 0.0002$. This very small efficiency loss of 0.6% has a negligible impact on the estimation of the polarization fluxes and the calibration error itself.

3.1. Polarization degree and angle estimates

In order to compare our results with low angular resolution CMB experiments, we present in Tab. 2 the Stokes I , Q , and U , the polarization intensity, polarization degree p and angle ψ . All the listed values are estimated inside apertures with radius of $5'$, $7'$ and $10'$ FWHM from the center of the map. The uncertainties account for the calibration error of 10%. The polarization angle is here presented in Equatorial coordinates and Galactic coordinates to ease the comparison with CMB experiments. The polarization angle uncertainty accounts for 2.3° systematic uncertainties, while the statistical uncertainties accounts also for

	I [Jy]	Q [Jy]	U [Jy]	I_{pol} [Jy]	p [%]	$\psi_{eq} (\psi_{gal})$ [$^\circ$]
5' FWHM centered	182.3 \pm 28.5	2.7 \pm 0.4	-15.3 \pm 1.3	15.4 \pm 1.6	8.5 \pm 0.9	140.0 (-82.4) \pm 0.2 \pm 0.5 \pm 1.8*
7' FWHM centered	215.7 \pm 27.9	3.2 \pm 0.5	-14.1 \pm 1.1	14.5 \pm 1.4	6.7 \pm 0.7	141.4 (-83.8) \pm 0.5 \pm 0.5 \pm 1.8*
10' FWHM centered	209.9 \pm 27.1	3.2 \pm 0.5	-13.2 \pm 0.9	13.3 \pm 1.3	6.5 \pm 0.6	142.0 (-84.3) \pm 0.6 \pm 0.5 \pm 1.8*

Table 2. NIKA Crab nebula total flux I , Q , and U are here presented, estimated by using aperture photometry methods. Polarized intensity flux I_{pol} , polarization degree p , and angles ψ_{eq} (Equatorial coordinates) and ψ_{gal} (Galactic coordinates) within parenthesis, are also presented. The values have been calculated within 5', 7', 10', centered on the map center position. A total calibration error of 10 % has been accounted for and propagated to the polarization estimates. The statistical uncertainty accounts also for montecarlo simulation of the noise in Q and U and the differences between two sets of jack-knife maps, 7 each. *A systematic angle uncertainty of 1.8° must be considered in the polarization angle error budget. We also consider a 0.5° of uncertainty due to the intensity to polarization leakage correction.

Frequency [GHz]	I [Jy]	Q [Jy]	U [Jy]	I_{pol} [Jy]	p [%]	ψ_{gal} [$^\circ$]
100	229.23 \pm 0.69	-15.91 \pm 0.05	1.38 \pm 0.09	15.97 \pm 0.08	6.97 \pm 0.03	-87.52 \pm 0.12
143	195.07 \pm 1.44	-12.55 \pm 0.13	1.49 \pm 0.09	12.64 \pm 0.15	6.48 \pm 0.08	-86.61 \pm 0.32
217	171.36 \pm 0.88	-12.10 \pm 0.07	0.88 \pm 0.11	12.14 \pm 0.09	7.08 \pm 0.05	-87.93 \pm 0.19
353	143.20 \pm 1.08	-9.98 \pm 0.26	1.13 \pm 0.18	10.05 \pm 0.31	7.01 \pm 0.20	-86.76 \pm 0.81

Table 3. The same quantities as in Tab. 2 derived with the new analysis of HFI *Planck* results by using aperture photometry of the polarization maps published in [Planck Collaboration et al. \(2016b\)](#).

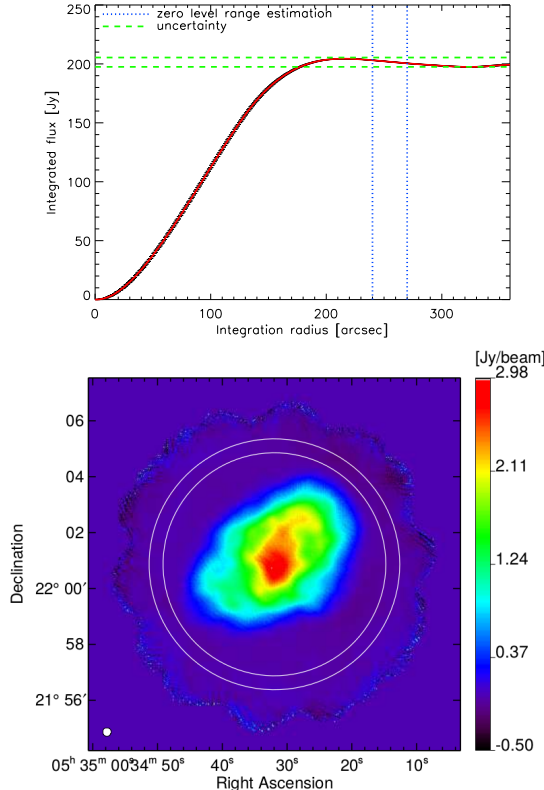


Fig. 5. Cumulative flux of the Crab nebula (top) obtained at 150 GHz over 4' from the center obtained by aperture photometry. The flux has been corrected by a zero level in the map, which corresponds to the mean of the signal calculated in an annular ring as indicated by the white circles on the map and by the blue dotted lines on the top. The green dotted line represents the uncertainties measured at large radii.

montecarlo simulation of the noise in Q and U and the difference between two sets of jack-knife noise maps, 7 maps each.

Fig. 6 shows the polarization fraction (top) and polarization angle (bottom) of the Crab nebula as a function of the frequency as measured by five different instruments: *WMAP* ([Weiland et al. 2011](#)), XPOL ([Aumont et al. 2010](#)), POLKA ([Wiese-](#)

[meyer et al. 2014](#)), *Planck* ([Planck Collaboration et al. 2016a](#)), and NIKA (this paper). Notice that *WMAP* satellite has FWHMs: 0.93° , 0.68° , 0.53° , 0.35° , and $<0.23^\circ$ at 22 GHz, 30 GHz, 40 GHz, 60 GHz, and 90 GHz respectively. XPOL and POLKA have FWHMs of $27''$ and $20''$, respectively. The *Planck* satellite FWHMs are: $33'$, $24'$, $14'$, $10'$, $7.1'$, $5.5'$, and $5'$ arcminutes at 30, 44, 70, 100, 143, 217, and 353 GHz, respectively. Furthermore, after discussions with the *Planck* team we have reanalysed the *Planck* HFI data using the polarization maps presented in [Planck Collaboration et al. \(2016b\)](#). We have performed aperture photometry directly in the Healpix maps. The results are given in Tab. 3.

The NIKA and POLKA values in Fig. 6 have been estimated by aperture photometry up to $10'$. XPOL value considers $10'$ ([Aumont et al. 2010](#)) and the other experiments their native FWHM. Using all the data sets we compute weighted-average of the polarization angle $\psi = -87.5^\circ \pm 0.3^\circ$. All the observations shown on the bottom panel of Fig. 6 agree within 1σ with this value except for NIKA and POLKA. We find a very good agreement between these two high angular resolution experiments and we also find that NIKA is consistent within 1σ with *Planck* value at 143 GHz and 2σ with the average value. The NIKA result differs from the average value by $\sim 3^\circ$. Referring to [Ritacco, A. et al. \(2017\)](#) a calibration angle error of 3° could explain the differences noticed on the calibration targets used between NIKA and other experiments. Despite the study on the Crab nebula evidences that a calibration factor on the polarization angle may affect our results, the results presented in [Ritacco, A. et al. \(2017\)](#) are still consistent within the error bars with the other experiments. Considering that NIKA is not anymore used we cannot conclude on this calibration error. However we also notice that if we consider only pixels with an I_{pol} SNR larger than 3 we find $-87.6^\circ \pm 0.1^\circ \pm 2.3^\circ$ (syst). This discrepancy could be explained by the fact that some of the pixels on the Q and U maps are biased by the noise.

Using all available data sets but POLKA results we have computed the weighted average degree of polarization and uncertainties on it. We find $6.95 \pm 0.03\%$ as shown by the solid line and dashed lines on the top panel of Fig. 6. We observe that most of the results between 20 and 353 GHz are consistent with this value at 1σ level, but *Planck* at 70 GHz, XPOL and POLKA that show a significantly larger degree of polarization.

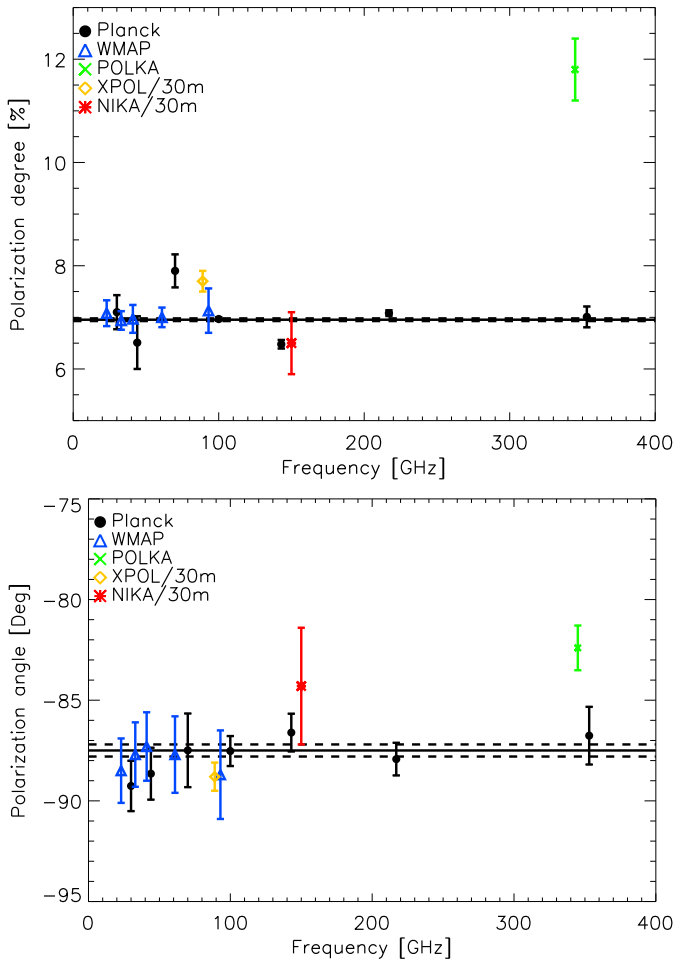


Fig. 6. Top: polarization degree as a function of frequency as measured by *Planck* (black dots), *WMAP* (blue triangles), *XPOL* (yellow diamond), *POLKA* (green cross) and *NIKA* (red crosses). The *NIKA* and *POLKA* values have been estimated by aperture photometry considering the source extension up to $10'$. Notice that *Planck* and *WMAP* values are shown at their native resolution. *XPOL*, *NIKA* and *POLKA* values have been integrated over the source. The solid line represents the weighted-averaged degree for all experiments but *POLKA*. Dashed lines represent 1σ uncertainties. Bottom: polarization angles in Galactic coordinates for the same five experiments given above. The solid line represents the weighted-averaged polarization angle computed using all the values.

For *XPOL* the discrepancy can probably be explained by the lower sensitivity of the single channel *XPOL* experiment to the lower than average polarization of the outer parts of the nebula. *POLKA* shows a very high polarization degree due to the $\sim 40\%$ flux loss observed in Stokes I , see Fig. 7. This is compatible with the losses expected due to the spatial filtering of total intensity in LABOCA data reduction in this range of angular scales (Belloche et al. 2011).

In the case of *Planck* HFI, we only find significant discrepancies for the 143 GHz data that remain unexplained to date.

The constant behaviour of the polarization degree over a large frequency range implies that the polarization emission is driven by the same physical process. As a consequence we expect a constant behaviour of the spectral index in polarization. Next section will discuss the characterization of the Spectral Energy Distribution in total power and polarization as well.

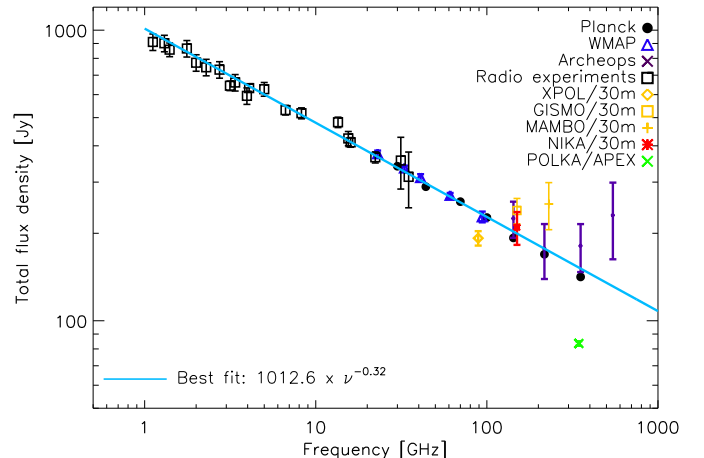


Fig. 7. Crab nebula total power SED as obtained from *Planck* (Planck Collaboration et al. 2016a) for the LFI instrument, *Planck* HFI data reanalysed from the maps published in Planck Collaboration et al. (2016b), *WMAP* (Weiland et al. 2011), *Archeops* (Macías-Pérez et al. 2007), radio experiments (Dmitrenko et al. 1970; Vinogradova et al. 1971), *XPOL*/30m (Aumont et al. 2010), *NIKA*/30m (this paper), *MAMBO*/30m (Bandiera et al. 2002), *POLKA*/*APEX* (Wiesemeyer et al. 2014) and *GISMO*/30m (Arendt et al. 2011) data. *NIKA* and *POLKA* values are estimated over the entire extend of the source. The best-fit single power law model obtained by the analysis in this paper is shown in cyan. Both, the best-fit models and the data account for the Crab nebula fading with time, using 2018 as year of reference. The *POLKA* data flux loss ($\sim 40\%$) is compatible with the losses expected due to the spatial filtering of total intensity in LABOCA data reduction (Belloche et al. 2011).

4. Characterization of the Crab Spectral Energy Distribution in intensity and polarization

4.1. Intensity

The total flux density of the Crab nebula at radio and millimeter wavelengths (from 1 to 500 GHz) is mainly expected to be due to synchrotron emission and can be well described by a single power law of the form:

$$I_\nu = A(\nu/1\text{GHz})^\beta \quad (4)$$

with spectral index $\beta = -0.296 \pm 0.006$ (Baars et al. 1977; Macías-Pérez et al. 2010). Further, the emission of the Crab nebula is fading with time at a rate of $\alpha = -0.167 \pm 0.015\% \text{ yr}^{-1}$ (Aller & Reynolds 1985). These results suggest a low frequency emission produced by particles accelerated by the same magnetic field. Macías-Pérez et al. (2010) have shown also that there is no evidence for an extra synchrotron component nor for thermal dust emission at these frequencies. The direction of the polarization is therefore expected to be constant across the frequency range 30–300 GHz while the polarization degree may vary.

Fig. 7 shows the total flux density of the Crab nebula as a function of the frequency. The fluxes in the radio domain were taken from Dmitrenko et al. (1970) and Vinogradova et al. (1971). We also show microwave and mm wavelengths fluxes from *Archeops* (Macías-Pérez et al. 2007), *Planck* (Planck Collaboration et al. 2016a), *WMAP* (Weiland et al. 2011), *XPOL*/30m (Aumont et al. 2010), *MAMBO*/30m (Bandiera et al. 2002), *POLKA* (Wiesemeyer et al. 2014) and *GISMO*/30m (Arendt et al. 2011). The HFI *Planck* data have been recomputed, from the maps published in Planck Collaboration et al. (2016b), because of flux loss observed in previous results. These new results will be soon published by the *Planck* collaboration. The

measured *NIKA* total flux density at 150 GHz is shown in red. Notice that in the plot both the best-fit model and the data represented are corrected for the fading of the source.

Assuming the single power law model in Eq. 4 and by χ^2 -minimization we obtain:

$$A = 1012.6 \pm 3.8 \text{ Jy}; \quad \beta = -0.324 \pm 0.001$$

The best-fit model is shown in Fig. 7 in cyan. The *NIKA* data are consistent with this model at 1σ level. The estimated spectral index β is slightly different from previous results provided by Macías-Pérez et al. (2010). This is probably due to the addition of new *Planck* and WMAP data.

As already discussed above, XPOL total power emission is low with respect to expectations. The POLKA value is found lower than *Planck* result at the same frequency, this is mainly explained by the spatial filtering of LABOCA data reduction as already discussed in the previous section.

4.2. Polarization

Though the total power emission of the Crab nebula has been monitored over decades across a large range of frequencies, the amount of polarization data is still lacking. Recent results provided by *Planck* (Planck Collaboration et al. 2016a) for LFI instrument, *Planck* HFI data reanalysed from the maps published in Planck Collaboration et al. (2016b), WMAP (Weiland et al. 2011), XPOL (Aumont et al. 2010) and POLKA (Wiesemeyer et al. 2014), together with *NIKA* allow us to trace the spectral energy distribution of the polarized emission I_{pol} as shown in Fig. 8. Notice that the uncertainty for the *NIKA* value includes also absolute calibration errors. Assuming a single power law synchrotron emission, see Eq. 4, for the polarization emission of the Crab nebula and using χ^2 fitting procedure we find:

$$A_{pol} = 78.98 \pm 7.82 \text{ Jy}; \quad \beta_{pol} = -0.35 \pm 0.03$$

We observe that *NIKA*, XPOL and POLKA results are consistent with the best-fit model at the 1σ level. We have also estimated the spectral index of the Crab nebula polarization emission at high frequency using the map obtained by SCUPOL (Matthews et al. 2009) at 352 GHz (850 μm) and the *NIKA* map. Considering only the region observed by SCUPOL ($\sim 1.5'$) we obtain $\beta_{pol}^{NIKA/SCUPOL} = -0.33 \pm 0.01$. This result is in good agreement with the best-fit model spectral index presented above.

The polarization spectral index is consistent with the total power one confirming the synchrotron radiation as the fundamental mechanism that drives the polarization emission of the Crab nebula.

5. Conclusions

The Crab nebula is considered as a celestial standard calibrator for CMB experiments in terms of polarization degree and angle. An absolute calibration is particularly important for reliable measurements of the CMB polarization B-modes, which are a window towards the physics of the early Universe.

We have reported in this paper the first high angular resolution polarization observations of the Crab nebula at 150 GHz, obtained with the *NIKA* camera. These observations have allowed us to map the spatial distribution of the polarization fraction and angle.

Using the *NIKA* data, in addition to all available polarization data to date, we conclude that the polarization angle of the Crab

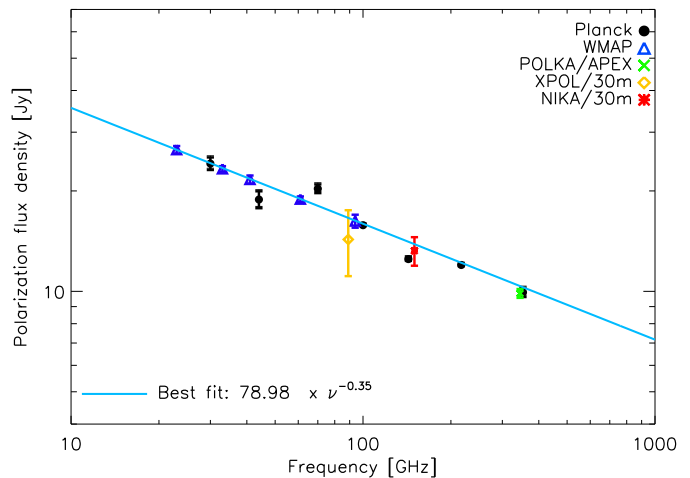


Fig. 8. Crab nebula polarization flux SED as obtained from *Planck* LFI (Planck Collaboration et al. 2016a), *Planck* HFI data reanalysed from the maps published in Planck Collaboration et al. (2016b), WMAP (Weiland et al. 2011), XPOL (Aumont et al. 2010), POLKA (Wiesemeyer et al. 2014) and *NIKA* (this paper) data. *NIKA* and POLKA values are estimated over the entire extend of the source. Both, the best-fit models and the data account for the Crab nebula fading with time, using 2018 as year of reference. We also show the single power law best-fit model in cyan.

nebula is consistent with being constant with frequency, from 20 GHz to 353 GHz, at arcmin scales with a value of $-87.5^\circ \pm 0.3$ in Galactic coordinates. High resolution observations provided by *NIKA* at 150 GHz and POLKA at 345 GHz show a polarization angle $\sim 3^\circ$ lower than the average value. Though the uncertainties on these values are high because of the systematic errors, this discrepancy highlights the need of further high angular resolution polarization observations in this frequency range. In addition, we find a strong case for a constant polarization degree of $p = 6.95 \pm 0.03\%$.

Moreover, we have characterized the intensity and polarization SED of the Crab nebula. In both total power and polarization, we find that the data are overall consistent with a single power law spectrum as expected from synchrotron emission from a single population of relativistic electrons. We find that the Crab nebula presents a polarization spectral index which is consistent with the index in intensity. However, we find some discrepancies between data sets, which will require further mm measurements. Among future polarization experiments, *NIKA2* (Calvo et al. 2016), will provide high sensitive polarization observations of the Crab nebula adding a 260 GHz map at 11'' resolution.

References

- Adam, R., Adane, A., Ade, P. A. R., et al. 2018, A&A, 609, A115
- Adam, R., Comis, B., Macías-Pérez, J. F., et al. 2014, A&A, 569, A66
- Aller, H., & Reynolds, S. 1985, The Astrophysical Journal, 293, L73
- Arendt, R. G., George, J. V., Staguhn, J. G., et al. 2011, ApJ, 734, 54
- Aumont, J., Conversi, L., Thum, C., et al. 2010, A&A, 514, A70
- Baars, J., Genzel, R., Pauliny-Toth, I., & Witzel, A. 1977, Astronomy and Astrophysics, 61, 99
- Bandiera, R., Neri, R., & Cesaroni, R. 2002, A&A, 386, 1044
- Belloche, A., Schuller, F., Parise, B., et al. 2011, A&A, 527, A145
- Calvo, M., Benoît, A., Catalano, A., et al. 2016, Journal of Low Temperature Physics, 184, 816
- Catalano, A., Adam, R., Ade, P., et al. 2016, arXiv preprint arXiv:1605.08628
- Catalano, A., Calvo, M., Ponthieu, N., et al. 2014, A&A, 569, A9
- Dmitrenko, D., Tseytin, N., Vinogradova, L., & Giterman, K. F. 1970, Radiophysics and Quantum Electronics, 13, 649

- Hester, J. J. 2008, ARA&A, 46, 127
- Kuz'min, A. D. & Udal'Tsov, V. A. 1959, Soviet Ast., 3, 39
- Lobanov, A. P., Horns, D., & Muxlow, T. W. B. 2011, A&A, 533, A10
- Macías-Pérez, J., Lagache, G., Maffei, B., et al. 2007, Astronomy & Astrophysics, 467, 1313
- Macías-Pérez, J. F., Mayet, F., Aumont, J., & Désert, F.-X. 2010, ApJ, 711, 417
- Matthews, B. C., McPhee, C. A., Fissel, L. M., & Curran, R. L. 2009, ApJS, 182, 143
- Mayer, C. H., McCullough, T. P., & Sloanaker, R. M. 1957, ApJ, 126, 468
- Michel, F. C., Scowen, P. A., Dufour, R. J., & Hester, J. J. 1991, ApJ, 368, 463
- Monfardini, A., Adam, R., Adane, A., et al. 2014, Journal of Low Temperature Physics, 176, 787
- Monfardini, A., Benoit, A., Bideaud, A., et al. 2011, ApJS, 194, 24
- Monfardini, A., Swenson, L. J., Bideaud, A., et al. 2010, A&A, 521, A29
- Montier, L., Plaszczynski, S., Levrier, F., et al. 2015, A&A, 574, A136
- Moreno, R. 2010, Neptune and Uranus planetary brightness temperature tabulation, Tech. rep., ESA Herschel Science Center, available from <ftp://ftp.sciops.esa.int/pub/hsc-calibration/PlanetaryModels/ESA2>
- Planck Collaboration, Ade, P. A. R., Aghanim, N., et al. 2016a, A&A, 594, A26
- Planck Collaboration, Aghanim, N., Ashdown, M., et al. 2016b, A&A, 596, A107
- Ritacco, A., Adam, R., Adane, A., et al. 2016, Journal of Low Temperature Physics, 184, 724
- Ritacco, A., Ponthieu, N., Catalano, A., et al. 2017, A&A, 599, A34
- Simmons, J. F. L., Aspin, C., & Brown, J. C. 1980, A&A, 91, 97
- Simmons, J. F. L. & Stewart, B. G. 1985, A&A, 142, 100
- Thum, C., Wiesemeyer, H., Paubert, G., Navarro, S., & Morris, D. 2008, PASP, 120, 777
- Vinogradova, L. V., Dmitrenko, D. A., & Tsejtin, N. M. 1971, Izvestia Vysshiaia Uchebn. Zaved., Radiofizika, 14, 157
- Weiland, J. L., Odegard, N., Hill, R. S., et al. 2011, ApJS, 192, 19
- Weiler, K. W. & Panagia, N. 1978, A&A, 70, 419
- Weisskopf, M. C., Hester, J. J., Tenant, A. F., et al. 2000, ApJ, 536, L81
- Wiesemeyer, H., Hezareh, T., Kreysa, E., et al. 2014, PASP, 126, 1027
- Wiesemeyer, H., Thum, C., Morris, D., Aumont, J., & Rosset, C. 2011, A&A, 528, A11

Acknowledgements. We would like to thank the IRAM staff for their support during the NIKA campaigns. The NIKA dilution cryostat has been designed and built at the Institut Néel. In particular, we acknowledge the crucial contribution of the Cryogenics Group, and in particular Gregory Garde, Henri Rodenas, Jean Paul Leggeri, Philippe Camus. This work has been partially funded by the Foundation Nanoscience Grenoble, the LabEx FOCUS ANR-11-LABX-0013 and the ANR under the contracts “MKIDS”, “NIKA” and ANR-15-CE31-0017. This work has benefited from the support of the European Research Council Advanced Grant ORISTARS under the European Union’s Seventh Framework Programme (Grant Agreement no. 291294). We acknowledge fundings from the ENIGMASS French LabEx (R. A. and F. R.), the CNES post-doctoral fellowship program (R. A.), R.A. acknowledges support from Spanish Ministerio de Economía and Competitividad (MINECO) through grant number AYA2015-66211-C2-2, the CNES doctoral fellowship program (A. R.) and the FOCUS French LabEx doctoral fellowship program (A. R.). A.M. has received funding from the European Research Council (ERC) under the European Union’s Horizon 2020 research and innovation programme (Magnetic YSOs, grant agreement No 679937).